Laboratory data linking the reconfiguration of and drag on individual plants to the velocity structure and wave dissipation over a meadow of salt marshes under waves with and without current

Xiaoxia Zhang[1*], Heidi Nepf[2]

[1]Water Science and Environmental Engineering Research Center, College of Chemical and Environmental Engineering, Shenzhen University, Shenzhen, 518060, China

[2]Department of Civil and Environmental Engineering, Massachusetts Institute of Technology, Cambridge, Massachusetts, 02139, USA

Correspondence: Xiaoxia Zhang (xiaoxiazhang@szu.edu.cn)

Abstract

Salt marshes provide valuable ecosystem services, which are influenced by their interaction with current and waves. On the one hand, current and waves exert hydrodynamic force on salt marsh plants, which shapes the distribution of species within the marsh. On the other hand, the resistance produced by the plants can shape the flow structure, turbulence intensity, and the wave dissipation over the canopy. Because marsh plants are flexible structures, their reconfiguration modifies the drag felt by the plants and the flow. While several previous studies have considered the flexibility of the stem, few studies have considered the leaf component, which has been shown to contribute the majority of plant resistance. This paper reports a unique dataset that includes laboratory measurements of both the force on an individual plant and the flow structure and wave energy dissipation over a meadow of plants. In the individual plant experiment, the motion of the plant and plant drag, free surface displacement and velocity profile were measured. The individual plant experiments considered both a live marsh plant (*Spartina alterniflora*) and a mimic consisting of ten leaves attached to a central stem. For the meadow experiment, velocity profiles were measured both upstream and within the meadow, and free surface displacement was measured along the model marsh plant meadow with high spatial and temporal resolution. These experiments used five water depths (covering both submerged and emergent conditions), three wave periods (from long wave to short waves), seven wave heights (from linear to nonlinear waves), six current conditions (including pure current, pure wave, and combined current and waves). In summary, there are 102 individual plant tests and 58 meadow tests. The drag, free surface displacement, and velocity are reported in SMCW.mat file including the raw data, the phase averages, and the statistical values. A link to the plant motion videos is also provided. This dataset provides high quality measurements that can be used to develop and validate models of plant motion, hydrodynamic drag on individual plants, vegetation-generated turbulence, the evolution of flow structure through a meadow, and the transformation and dissipation of waves over natural salt marshes. The dataset is available from figshare with detailed instructions for reuse (https://doi.org/10.6084/m9.figshare.24117144; Zhang and Nepf, 2023a).

Keywords: salt marsh; flexible plant; drag force; reconfiguration; flow structure; wave dissipation;

1. Introduction

Salt marshes are a common feature of coastal and estuary regions, serving as important habitats and food sources for intertidal invertebrates and small fish (Boesch and Turner, 1984; Barbier et al., 2011). These marshes also play a crucial role in carbon sequestration, accumulating carbon stocks at a rate of 210 g/cm^2/year, the highest among all ecosystems on Earth (Pidgeon, 2009). Additionally, salt marshes provide shoreline protection by dissipating extreme waves (Zhang et al., 2020; Garzon et al., 2019b) and reducing erosion and enhancing sedimentation (Schoutens et al., 2019; Elschot et al., 2013; Huai et al., 2021). The health and function of salt marsh ecosystems depend on the interaction between the marsh and surrounding currents and waves. Currents and waves exert hydrodynamic forces on marsh plants, influencing the distribution of species within the marsh (Schoutens et al., 2022, 2020). In addition, because marsh plants are flexible, they reconfigure under hydrodynamic forces, modifying the forces experienced by the plants (Zhang and Nepf, 2021b), and the impact of plant resistance on flow structure (Chen et al., 2013; Lowe et al., 2005; Zeller et al., 2015; Lei and Nepf, 2021), turbulence intensity (Xu and Nepf, 2020), and wave energy transformation (Hu et al., 2014; van Veelen et al., 2020; Vuik et al., 2016).

Theories that quantify the hydrodynamic force on rigid cylinders and flat plates were developed in the 1950's (Morison et al., 1950; Keulegan and Carpenter, 1958). However, real plants are flexible and reconfigure under the influence of currents and waves, reducing the hydrodynamic forces they experience (Luhar and Nepf, 2011; Gosselin et al., 2010; Mullarney and Henderson, 2010; Zhu et al., 2020). Models have been developed to predict the forces on flexible structures by considering the reconfiguration and relative motion between the fluid and the plant (Luhar and Nepf, 2011; Mullarney and Henderson, 2010; Gosselin et al., 2010; Lei and Nepf, 2019b). Laboratory measurements have shown that real plants with different morphologies followed different scaling laws (Harder et al., 2004; Schutten and Davy, 2000; Jalonen and Järvelä, 2013; Whittaker et al., 2013; Zhang and Nepf, 2020). Many salt marsh plants consist of multiple flexible leaves attached to single, less flexible central stem, e.g., *Phragmites australis*, *Scirpus maritimus*, *Spartina alterniflora*, and *Spartina anglica*. For these plants, the rigidity and geometrical properties as well as the density of the leaves and stem affect the drag and hence the wave dissipation by the plants (Zhu et al., 2023). Zhang and Nepf (2021b) demonstrated that the force acting on a full model plant can be estimated by summing the forces on all the leaves and the stem, while applying a sheltering coefficient to account for the plant drag reduction due to the interaction and sheltering among the leaves and the stem. The sheltering coefficient depends on the geometrical properties of the plant (mainly the distribution of leaves on the stem) and does not vary with flow conditions. Based on this, predictive models were proposed to estimate the forces acting on salt marsh plants with both leaves and stem (Zhang and Nepf, 2021b, 2022).The plant rigidity, morphology, and spatial distribution vary significantly in the field, which makes the estimation of plant drag and wave dissipation difficult in practice. Fortunately, average values of plant properties have been shown to produce reasonable estimation for field measurements of wave dissipation (Zhang and Nepf, 2021b; Zhang et al., 2022, 2021; Zhu et al., 2023).

Within a canopy, the presence of plants can significantly alter the flow structure (Chen et al., 2013; Lowe et al., 2005; Zeller et al., 2015; Lei and Nepf, 2021) and turbulence intensity (Xu and Nepf, 2020), and reduce wave energy (Garzon et al., 2019a; Zhang et al., 2020; Maza et al., 2015). The fully developed flow structure within a canopy has been extensively studied under both current (Chen et al., 2013; Lei and Nepf, 2021) and wave conditions (Lowe et al., 2005) for both emergent and submerged canopies. Specifically, the mean flow is determined by the distribution of the plant frontal area for emergent canopies, and by the canopy drag and the ratio of water depth to plant height for submerged canopies (Nepf, 2012). The wave orbital velocity experiences less modification by a canopy due to the greater inertial force under waves compared to current (Lowe et al., 2005), which allows flow motion to penetrate deeper into the lower canopy region. The presence of plants affects turbulence intensity directly through form drag and wake generated by plant elements, and indirectly by adjusting the flow structure to create a greater shear and thus shear production (Nepf, 2012). The resistance of plants can reduce wave height by 30% to 90% over the first 30 m of a salt marsh (Ysebaert et al., 2011; Knutson et al., 1982; Zhang et al., 2020; Garzon et al., 2019a), depending on the plant properties (density, geometry, and mechanical characteristics) and flow conditions (water depth, wave period, wave amplitude, presence of current). Recent studies proposed simple predictions for wave decay over salt marshes under pure waves (Zhang et al., 2021, 2022), which has been extended to combined current and wave conditions using the in-canopy total velocity (Zhang and Nepf, 2021a). However, a well-validated theoretical model for the time-varying total velocity is currently lacking for salt marshes under combined current and waves, which hinders the development of accurate models for canopy turbulence and wave dissipation.

This paper presents both force measurements on individual salt marsh plants (Zhang and Nepf, 2021b, 2022) and measurements of flow structure and wave decay along a meadow of salt marsh plants (Zhang et al., 2021, 2022; Zhang and Nepf, 2021a). The experiments utilized model plants that consisted of multiple flexible leaves attached to a central stem, which were designed to be geometrically and dynamically similar to *Spartina alterniflora*. The *Spartina spp*. family is distributed widely along the coasts of the Eastern United States, Europe, South America, and China (see the global distribution in figure 1B in Borges et al., 2021). The test conditions varied from submerge to emergent, from long to short waves, and from linear to nonlinear waves with and without following currents. In total, 102 individual plant tests and 58 meadow tests were conducted.

2. Method

The experiments were conducted in the Nepf Fluid Mechanics lab at MIT in a 24-m-long, 38-cm-wide, 60-cm-tall water channel (Fig. 1). The individual plant experiments (denoted by IE, Fig. 1a) provided synchronized measurements of plant drag and free surface displacement, as well as 3-dimensional velocity profiles provided as raw data, phase-averaged data, and statistical data. Additionally, a link to videos capturing the motion of the plants are provided. The meadow experiments (denoted by ME, Fig. 1b) provide time-varying measurements of free surface displacement along the meadow at 10 and 15 cm intervals, as well as velocity profiles upstream of and within the meadow with 1 to 2 cm vertical resolution. This dataset can facilitate the development and validation of dynamic marsh plant models, enhance predictions of marsh plant drag, and deepen our understanding of vegetation-induced turbulence, the evolution of flow structure within a canopy, and the transformation and dissipation of waves in natural salt marshes.

Monochromatic waves were used in all cases, with waves generated with a piston-type wavemaker. A beach with 1:5 slope and covered with a layer of 10-cm thick coconut fiber was located at the downstream end of the channel, which limited the wave reflection to 7% ± 3% for the tested conditions. Following currents (propagating in the same direction as the waves) were generated by a variable speed pump. Two bricks elevated the beach by 9 cm above the bed to allow the current to pass.

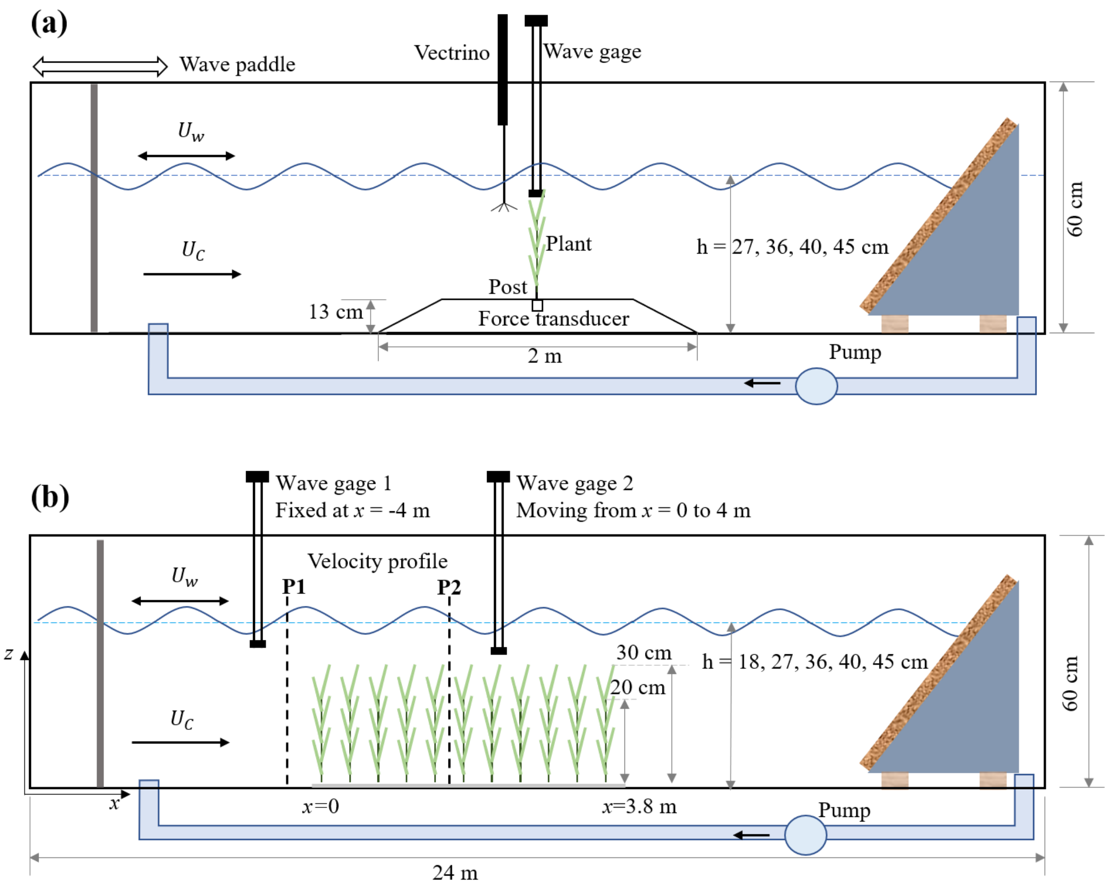

Fig. 1 Schematic of (a) the individual plant experiment (IE) and (b) the meadow experiment (ME), not to scale. The wave paddle and current inlet are at the left, and the wave-absorbing beach at the right. In subplot (a), the model plant was attached to a submersible force sensor housed in a 13-cm high acrylic ramp. A wave gage recorded the free surface displacement at the same longitudinal position as the plant, but 9 cm to the side. A Nortek Vectrino+ measured velocity 10-cm upstream of the plant position, but with the plant removed. In subplot (b), the model meadow was 3.8 m long and located at mid-length along the flume. Two wave gages measured the wave height at a stationary reference position (wave gage 1) and at multiple positions along the meadow (wave gage 2). Velocity in front (P1) and inside the meadow (P2) was measured by Vectrino+.

2.1 Individual plant experiment setup

The individual plant experiments (IE) tested a live *Spartina alterniflora*, a single flat plastic leaf, a single cylindrical stem, and a full model marsh plant consisting of 10 leaves attached to a central stem. These tests are labeled as live, leaf, stem, and model, respectively. Fig. 2 shows the live and model plants with the corresponding plant properties (see also Figure 2 and Table 1 in Zhang and Nepf, 2021). The live plant consisted of 5 leaves, the dimensions shown in Fig. 2a are the mean ± SD of these leaves. The plant was attached to a stainless steel post with 2 mm diameter. The length of the post above the ramp was l_p = 3, 4.5, 2, and 2 cm for the live, leaf, stem, and model plant, respectively. The lower part of the post was attached to a submersible force sensor (Futek LSB210 100g), which was mounted beneath an acrylic ramp (1-m top length, 2-m bottom length, 13-cm height, and spanning the flume width, see Fig. 1a) to avoid interaction between fluid motion and the sensor. IE measured the hydrodynamic force exerted on the plant, the motion of the plant, and the associated hydrodynamic conditions (velocity profile and wave height). The wave gauge was mounted at the same longitudinal position as the plant, but 9 cm to the lateral side. Note that for each plant and each water depth, the zero position of the wave gauge and force sensor was determined for still water, i.e., before the wave generator and current pump were turned on.

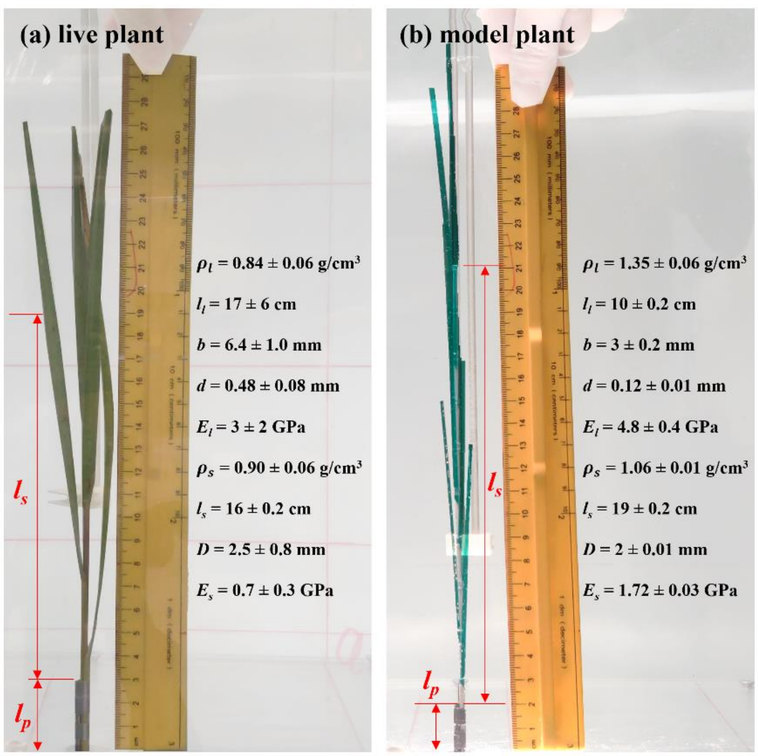

Fig. 2 Photos showing (a) the live plant and (b) model plant in the individual plant experiment (IE), including a list of plant properties. ρ is the plant material density, the subscript l and s denote parameters for the leaves and stem, respectively. E is the elastic modulus, l is the element length, b and d are the width and thickness of the leaf. D is the stem diameter.

IE tested 4 water depths $h = 27$, 36, 40, and 45 cm for the live and full model plant. The leaf and stem only tests were done under $h = 45$ cm. Note that the leaf data reported here corresponds with an initial vertical leaf posture, and the leaf width was oriented perpendicular to the wave propagation direction (i.e., leaf posture 1 in Figure 4a in Zhang and Nepf, 2021b). Three wave periods, T_w =2.01, 1.44, and 1.12 s, and six wave amplitudes were tested. All the tested conditions are summarized in Table 1, with the case names formed from the type of plant (Live, Leaf, Stem, Model), the water depth (h27, h36, h40, h45), the wave frequency (f05, f07, and f09), and the wave height level (W1, W2, W3, W4, W5, W6, W7, a_w ranging from 0.9 to 4.9 cm). The current conditions were labeled by pump frequency (10 to 50 Hz), C1, C2, C3, C4, and C5. For example, Leaf_h45_f05_C1W1 corresponds to the test for an individual model leaf with water depth $h =$ 45 cm, and wave period T_w =2.01 s (wave frequency is 0.5 Hz), current pump frequency set to 10 Hz and the smallest wave height (wave amplitude $a_w \approx 1$ cm). The tests include the pure wave experiment reported in Zhang and Nepf (2021) and the combined current and wave experiments reported in Zhang and Nepf (2022). In addition, there are 23 unreported cases labeled with bold font case names in Table 1 (6 model plant cases and 17 live plant tests). The new live plant tests included emergent conditions, which can be used to explore the plant drag dependence on the degree of submergence. The new model plant cases included a stronger wave condition ($a_w = 4.7$ cm) and five conditions within the published range of wave height. These new cases expanded the range of published flow conditions. Across the IE tests, the wave orbital velocity spanned $U_w = 4$ to 24 cm/s, and the channel-average current spanned $U_c = 3$ to 18 cm/s. The current to wave velocity ratio spanned $U_c/U_w = 0.16$ to 4.7, covering a range of conditions present in the field (Garzon et al., 2019b).

Table 1 IE case names with the measured wave amplitudes and the setting current velocity

case names	a_w ± 0.1 cm							U_c ± 0.1 cm/s
Live_h27_f05_W1/W2/W3/W4/W5	1.1	1.8	2.6	1.8	2.3			0
Live_h36_f05_W1/W2/W3/W4/W5/W6/W7	1.0	1.5	2.1	2.9	1.9	2.4	3.0	0
Live_h40_f05_W1/W2/W3/W4/W5	1.0	1.6	2.4	3.2	4.1			0
Live_h45_f05_W1/W2/W3/W4/W5	1.0	1.6	2.0	2.7	3.7			0
Leaf_h45_f05_W1/W2/W3/W4/W5	1.1	1.7	2.4	3.2	4.1			0
Stem_h45_f05_W1/W2/W3/W4/W5	1.0	1.7	2.4	3.3	4.1			0
Model_h27_f05_W1/W2/W3/**W4**/**W5**	1.3	2.0	2.7	2.0	2.5			0

Model _h36_f05_W1/W2/W3/W4/**W5**/**W6**/**W7**	1.0	1.6	2.2	3.1	2.0	2.5	3.1	0
Model _h40_f05_W1/W2/W3/W4/**W5**	1.1	1.7	2.4	3.4	4.7			0
Model _h45_f05_W1/W2/W3/W4/W5	0.9	1.5	2.5	3.8	4.2			0
Model _h45_f05_C1W1/W2/W3/W4/W5	1.2	2.0	2.9	4.1	5.2			3.0
Model _h45_f05_C2W1/W2/W3/W4/W5	1.2	2.1	3.0	4.2	5.3			6.8
Model _h45_f05_C3W1/W2/W3/W4/W5	1.2	2.1	3.0	4.1	4.9			10.1
Model _h45_f05_C4W1/W2/W3/W4/W5	1.0	1.7	2.6	3.7	4.8			13.7
Model _h45_f05_C5W1/W2/W3/W4/W5	1.2	2.1	3.0	4.1	5.2			17.6
Model _h45_f07_W1/W2/W3/W4/W5	1.5	2.2	3.1	4.1	6.3			0
Model _h45_f07_C2W1/W2/W3/W4/W5	1.6	2.3	3.2	4.1	6.1			6.8
Model _h45_f07_C4W1/W2/W3/W4/W5	1.1	1.8	2.8	3.7	6.1			13.7
Model _h45_f09_W5	3.0							0
Model _h45_f09_C2W5	2.6							6.8
Model _h45_f09_C4W5	2.2							13.7

The force sensor and wave gauge were controlled by a Labview program which enabled high quality synchronous measurement. Both the drag force and wave height were measured at a sampling rate of 2000 Hz and for a duration of 3 minutes. During the force and wave gauge measurements, a smart cellphone (MIX 2S) camera recorded a 10-second UHD 4k video at 30 fps, which covered 5 to 10 wave periods, depending on the wave period. The camera was fixed to a tripod such that the videos for each plant have the same window. The videos for all tests are available at: https://doi.org/10.6084/m9.figshare.24117324. After the force measurements, the plant and force sensor were removed, and a Nortek Vectrino+ was used to measure the velocity profile 10 cm upstream of the position where the plant had been to avoid the hole through which the plant was attached. The vertical resolution of the velocity profile was 1 cm. At each measurement point, the Vectrino recorded a 3-min record at 200 Hz.

2.2 Meadow experiment setup

In the meadow experiment (ME), the same model plants used in IE (Fig. 2b) were arranged in a staggered array with a meadow density of 280 plants/m^2 (Fig. 3). Once inserted, the erect plants were 30-cm tall. The plants were distributed across the channel width and over a streamwise distance of 3.8 m.

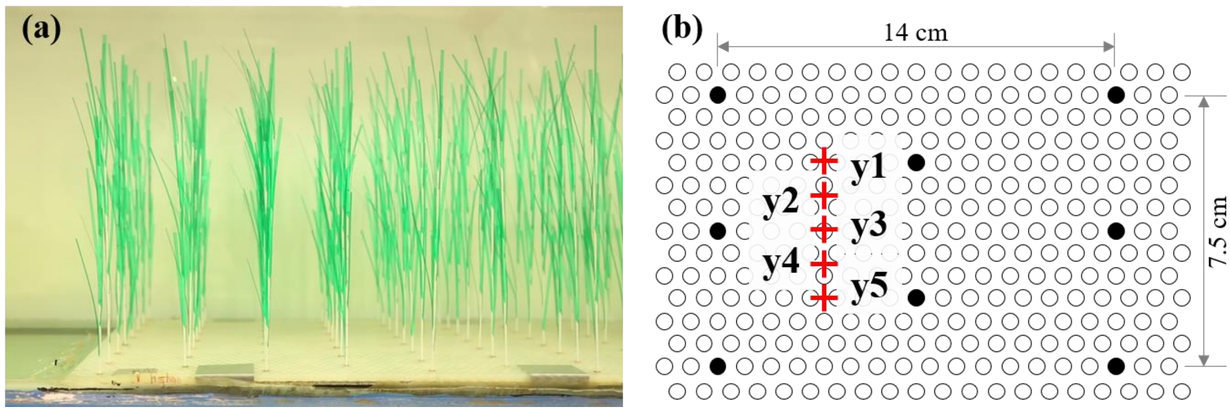

Fig. 3 a) Photo of the model plants, b) section of the baseboard with staggered holes (circles) and the plant positions within the hole array (filled circles)

ME tested five water depths, h = 18, 27, 36, 40, and 45 cm, three wave periods, T_w =2, 1.4, and 1.1 s, five wave amplitude levels, and three current magnitudes. All the ME cases were summarized in Table 2 with the case names formed based on the flow conditions in the same way as IE cases. The flow types include pure current, pure wave, and combined current and wave, which were labelled as PC, PW, and CW, respectively. In each case, two wave gages were synchronized to measure the free surface displacement at a reference position (wave gauge 1 at x = -4 m) and at positions along a transect through the canopy (wave gauge 2). During each experimental run (about 90 min), the wave amplitude at wave gage 1 varied by less than 3%, confirming stationary wave conditions. Wave gage 2 collected data between x = -4 to 4 m at 10 and 15 cm intervals. The leading edge of the meadow was located at x = 0, such that x < 0 was over bare bed. At each position, the free surface displacement, $\eta(t)$, was recorded at 2000 Hz for 1 minute. Additional measurements of wave amplitude were made without plants to assess the wave decay associated with the channel wall and baseboards alone.

Table 2 ME case names with the measured wave amplitudes and the setting current velocity

Flow	case names	aw ± 0.1 cm	Uc ± 0.1 cm/s
PC	h18_C1/C2/C3	/	4.7/7.8/10.1
PC	h27_C1/C2/C3	/	4.2/7.2/14.2
PC	h40_C1/C2/C3	/	4.6/7.6/12.7
PW	h18_f07_W1/W2/W3	1.0/1.6/2.3	0
PW	h27_f07_W1/W2/W3/W4/W5	1.0/1.6/2.3/3.0/4.1	0
PW	h36_f07_W1/W2/W3/W4/W5	1.0/1.6/2.3/3.0/4.2	0

PW	h40_f07_W1/W2/W3/W4/W5	1.0/1.5/2.3/3.0/4.1	0
PW	h45_f05_W1/W2/W3/W4/W5	0.9/1.5/2.1/3.0/4.0	0
PW	h45_f07_W1/W2/W3/W4/W5	1.0/1.5/2.2/2.9/4.0	0
PW	h45_f09_W1/W2/W3/W4/W5	0.9/1.5/2.2/3.1/4.1	0
CW	h18_f07_C1W1/W3	1.1/2.6	4.7
CW	h18_f07_C2W1/W3	1.0/2.5	7.8
CW	h27_f07_C1W1/W3/W4	1.0/2.3/3.1	4.2
CW	h27_f07_C2W1/W3/W4/W5	1.1/2.3/3.2	7.2
CW	h40_f07_C1W3/W4/W5	2.2/3.1/4.0	4.6
CW	h40_f07_C2W3/W4/W5	2.2/3.1/4.0	7.6

Two Nortek Vectrino+ were used to measure the vertical profiles of velocity with 1 to 2 cm vertical resolution at P1 (upstream of the meadow) and P2 (within the meadow) (Fig. 1b). At each measurement point, the Vectrino+ recorded a 1-min record with a sampling frequency of 200 Hz. Upstream of the meadow velocity was measured at the channel centerline. Inside the meadow, velocity measurements were made at one (y2 or y4 in Fig. 3b, as in Zhang et al., 2022, 2021) or five lateral locations near the flume centerline (red pluses in Fig. 3b, as in Zhang and Nepf, 2021a).

2.3 Data analysis

The free surface displacement, force, and velocity data were processed in a similar fashion. First, the analysis of wave data will be described in detail. The wave gauge has an accuracy of 0.2 (0.7) mm on average (maximum) based on the standard deviation of the raw data under still water conditions. For each record, the mean surface position was removed from the time series to obtain the free surface displacement data η. The surface displacement time series was separated into phase bins following (Lei and Nepf, 2019b; Zhang and Nepf, 2021a). Specifically, for sampling duration T, a wave measurement record contains $M = \mathrm{floor}(T/T_w)$ wave periods, with $\mathrm{floor}()$ denoting a downward rounding function. Each wave period contains $\gamma = T_w f_s$ samples and thus γ phase bins. f_s is the sampling frequency. The phase-averaged free surface displacement in the n^{th} phase bin ($n = 1$ to $\mathrm{floor}(\gamma)$), corresponding to phase $\phi = 2\pi n/\gamma$, was defined as,

$$\breve{\eta}\big(\phi(n)\big) = \frac{1}{M}\sum_{m=0}^{M-1}\eta(n+\gamma m) \quad (1)$$

$\breve{}$ denotes the phase-averaged value. Within each phase bin, the standard deviation of $\breve{\eta}$ was 0.7 (3.6) mm on average (maximum) based on the IE tests. Increasing current intensity led to higher uncertainty in $\check{\eta}$. The wave amplitude a_w was calculated from the root-mean-square surface displacement,

$$a_w = \sqrt{\frac{2}{\gamma}\sum_{\mathrm{n}=1}^{\gamma} \check{\eta}\big(\phi(n)\big)^2} \tag{2}$$

For ME, the spatial evolution of wave amplitude can be used to estimate the wave damping by vegetation. However, note that the wave amplitude reflected the sum of the incoming wave and the beach-reflected wave, the superposition of which resulted in an amplitude modulation at an interval of λ/2 (with wavelength λ, e.g., Fig. 4). Accounting for the wave modulation, the wave decay coefficient K_{Df} was estimated by fitting the measured amplitudes (Lei and Nepf, 2019b),

$$\frac{1}{a_{w,x}} = K_{Df}x + C_1\cos(2kx + \epsilon) + C_2 \tag{3}$$

in which $k = 2\pi/\lambda$ is the wavenumber, and ϵ, C_1, and C_2 are fitting parameters. Examples are shown in Fig. 4. Wave decay attributed to the plants (K_D [m^{-2}]) was obtained by subtracting the decay coefficient obtained in the flume without plants.

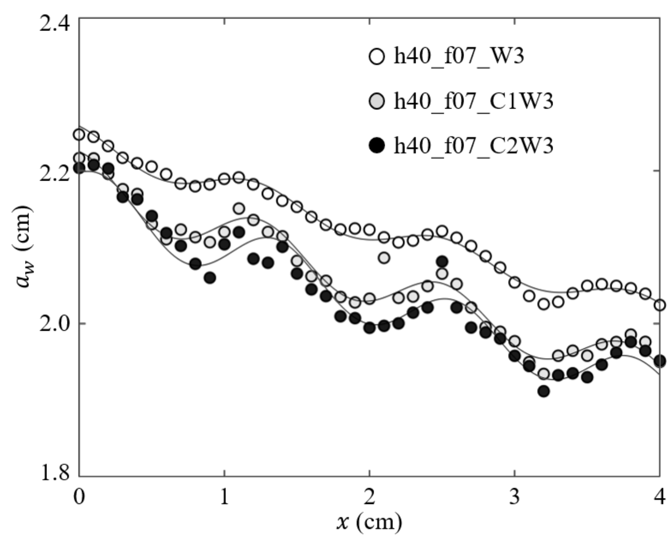

Fig. 4. Measured wave amplitude (symbols) and the fitted Eq. 3 (curves) for h40_f07_W3, h40_f07_C1W3, and h40_f07_C2W3 with the similar wave amplitude but increasing current. (adapted from Figure 4 in Zhang and Nepf, 2021a)

For the individual plant experiments, a time lag of *dt* = 74 ± 4 ms (SD) was determined between the force sensor and wave gauge due to the difference in the instruments' reaction time. This time lag was accounted for by removing the free surface displacement records (about 148 data points) before the first force sensor record. The FFT (fast Fourier transform) function in

MATLAB was used to filter out high-frequency noise (frequency components greater than 2 Hz), which was negligible based on the frequency spectrum and was subtracted from the raw data. The plant force time series, F, was obtained by removing the offset measured with still water conditions. The phase-averaged plant drag, $\breve{F}$, was obtained in similar way as Eq. 1. The maximum, minimum, and mean value of $\breve{F}$ are reported as F_{max}, F_{min}, and F_m, respectively. For pure current conditions, F_m, was defined by the average over the 3-minute record.

Based on the standard deviation among ten still water measurements, considering different water depth and different plants installed on the force sensor, the accuracy of the force measurements was determined to be 0.001 N (0.002 N) average (maximum). The force exerted on the post alone (without plant) was less than 3% of the force on the model plant (Zhang and Nepf, 2021b, 2022). Consequently, in this dataset, the force due to the post was neglected and not subtracted from the measurements. However, note that the force on the post can contribute up to 30% of the total force measured for an individual leaf. Hence, when using the leaf force data, it may be necessary to exclude the force due to the post.

For all velocity data, two despiking methods were applied to identify abnormal data points, which were replaced by a NAN (not a number) value. First, data points were identified if the associated acceleration exceeded the gravitational acceleration. Second, a threshold, ± 3σ with σ the standard deviation, was applied to identify abnormal data within each phase bins for conditions with waves and in the whole time series for the pure current cases (Zhang and Nepf, 2022). The despiked velocity data is denoted u, v, w, respectively, for the longitudinal, lateral, and vertical directions. For the horizontal velocity component, the velocity data was separated into a phase averaged value $\breve{u}(\phi)$ and a turbulent velocity fluctuation u',

$$u = \breve{u}(\phi) + u' = u_m + \breve{u}_w(\phi) + u' \tag{4}$$

$\breve{u}(\phi)$ was calculated in the same manner as Eq. 1, and then further separated into a time mean velocity $u_m = \frac{1}{2\pi}\int_0^{2\pi} \breve{u}(\phi)d\phi$ and a wave orbital velocity $\breve{u}_w(\phi) = \breve{u}(\phi) - u_m$. The magnitude of wave orbital velocity was defined as

$$u_w = \sqrt{2\frac{1}{2\pi}\int_0^{2\pi}(\breve{u}_w(\phi))^2 d\phi} \tag{5}$$

The root mean square of the fluctuating velocity component within each phase bin (e.g., $u_{rms} = \sqrt{\frac{1}{n}\sum_1^n u'^2}$) was used to estimate the turbulent kinetic energy in that phase bin, $tke\ (\phi) =$

$(u_{rms}{}^2 + v_{rms}{}^2 + w_{rms}{}^2)/2$. The time-average turbulent kinetic energy, TKE, was defined as the average of $tke(\phi)$ over all phases. The depth- and phase-averaged horizontal velocity was defined as $\breve{U} = \frac{1}{h}\int_0^h \breve{u}(\phi, z)dz$. The depth-average velocity statistics reported for each velocity profile includes the maximum U_{max}, minimum U_{min}, and mean U_m value of $\breve{U}$. The depth-average wave orbital velocity was defined as $U_w = \sqrt{2\frac{1}{2\pi}\int_0^{2\pi}(\breve{U} - U_m)^2 d\phi}$. For pure current cases, $U_m = U_c$ was defined by the depth- and time-averaged velocity over all measurements. The phase-averaged and depth-averaged values for the lateral (v) and vertical (w) velocity components were calculated in the same way as the horizontal component.

3. Data

3.1 Data for the individual plant experiments (IE)

In experiments with individual plants, the plant force and free surface displacement at the same streamwise (x) location as the plant were measured simultaneously. The motion of the plant was captured in videos during the force measurement. The flow velocity was measured separately, but assumed to be in-phase with the free surface displacement. These data contained all relevant parameters necessary for understanding the hydrodynamic performance of an individual marsh plant. For example, Fig. 5 shows the maximum plant motion, phase-averaged plant drag and free surface displacement, as well as the phase- and depth-averaged velocity for the model plant under the same wave with and without following current. These data demonstrate a strong dependence of plant force on the instantaneous flow velocity, which can be utilized to validate predictions of plant drag, as in Zhang and Nepf (2022, 2021b). It is worth noting that the phase-averaged data allows for detailed validation of phase resolving models. Only a few studies, e.g., Jacobsen et al. (2019); Luhar and Nepf (2016), have reported time-varying velocity and force on flexible plants. However, for modeling and validating plant motion and time-varying plant force, high-resolution time-varying horizontal and vertical velocity are required. For example, Zhu et al. (2020) demonstrated that the vertical velocity results in asymmetric plant motion, even when subjected to symmetric waves. For high resolution model validation, the present dataset includes both the time-varying horizontal and vertical velocity, as well as the synchronized force and free surface displacement for both live and model plants.

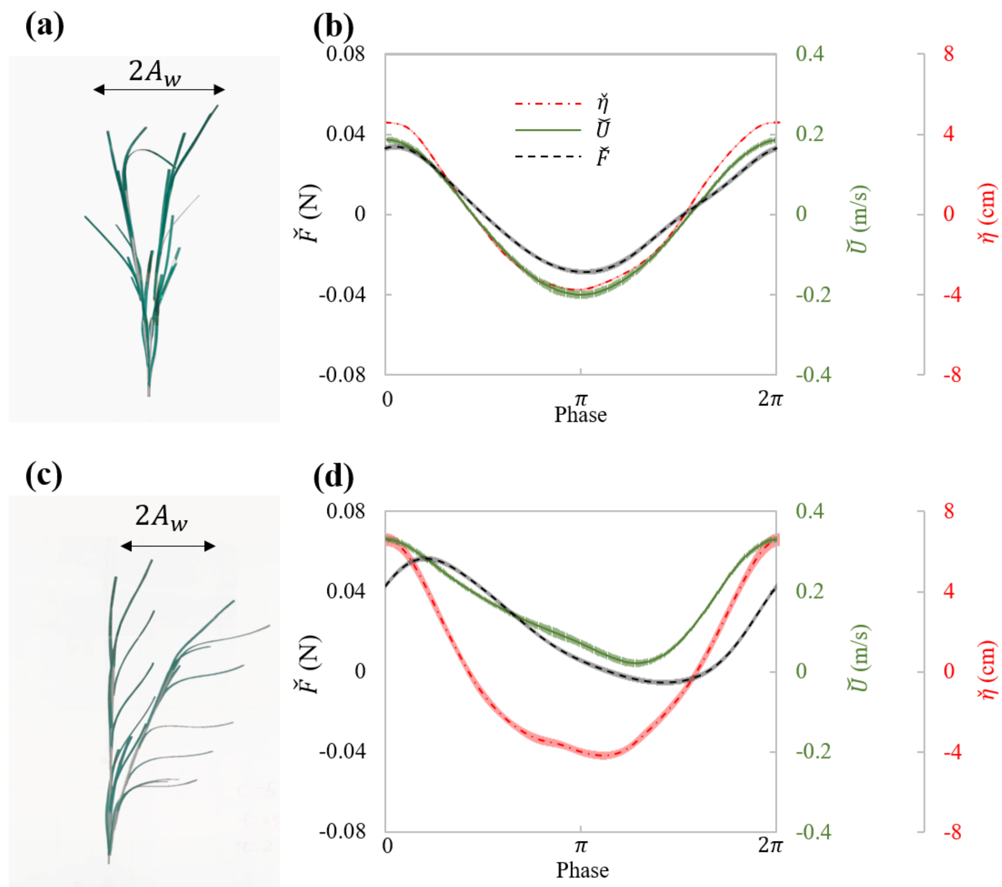

Fig. 5 Plant motion and phase-averaged measurements of force (black curve), surface displacement (red curve) and velocity (green curve) for (a) and (b) model_h45_f05_W5 (U_m = -1.9 cm/s, and U_w = 19.1 cm/s); and (c) and (d) model_h45_f05_C5W5 (U_m = -16.3 cm/s, and U_w = 14.3 cm/s). (a) and (c) showed the digital image of model plant at the maximum downstream and upstream posture within the wave cycle. The thin shading in each curve in subplots (b) and (d) indicate the uncertainty in each phase. (modified based on figure 5 in Zhang and Nepf, 2022).

The force measurements suggested that the force on the full plant was smaller than the sum of forces on all the leaves and stem acting alone, suggesting that sheltering and interaction among the leaves and stem decreased the force exerted on the full plant compared to the leaves and stem in isolation (Fig. 6a). The decrease in plant drag can be represented by a constant sheltering coefficient C_s for a given plant morphology. Specifically, for a plant with N_l leaves attached to a central stem, the force of on the full plant is: F (plant) = C_s × F (one leaf)× N_l + F (stem), with C_s =0.6 for the model plant reported here (Zhang and Nepf, 2021b). The leaves was estimated to contributed 72% ± 1% of the plant-scale drag (Zhang and Nepf, 2021b). With this finding, the hydrodynamic force on a plant with complex leaf and stem morphology can be easily estimated using the force prediction for an individual simple structure (a flat leaf or a cylindrical stem, e.g., the models described in Zhu et al., 2020; Mullarney and Henderson, 2010; Luhar and Nepf, 2011, 2016)).

The maximum force on the plant is plotted against the maximum depth- and phase-averaged velocity in Fig. 6. Note that for h = 40 and 45 cm, both the live and model plant were submerged at the wave crest (see videos in https://doi.org/10.6084/m9.figshare.24117324). The maximum force for these two water depths followed the same trend with velocity (Fig. 6b and c). For smaller water depth, only part of the plant was submerged, such that the plant felt smaller force under similar horizontal velocity (Fig. 6b and c). The relationship between F_{max} and U_{max} was similar for different current velocity, but curves were shifted to the right as current increased (darker symbols in Fig. 6d), i.e., as current magnitude increased, a greater U_{max} was needed to reach the same F_{max} (Fig. 6 d).

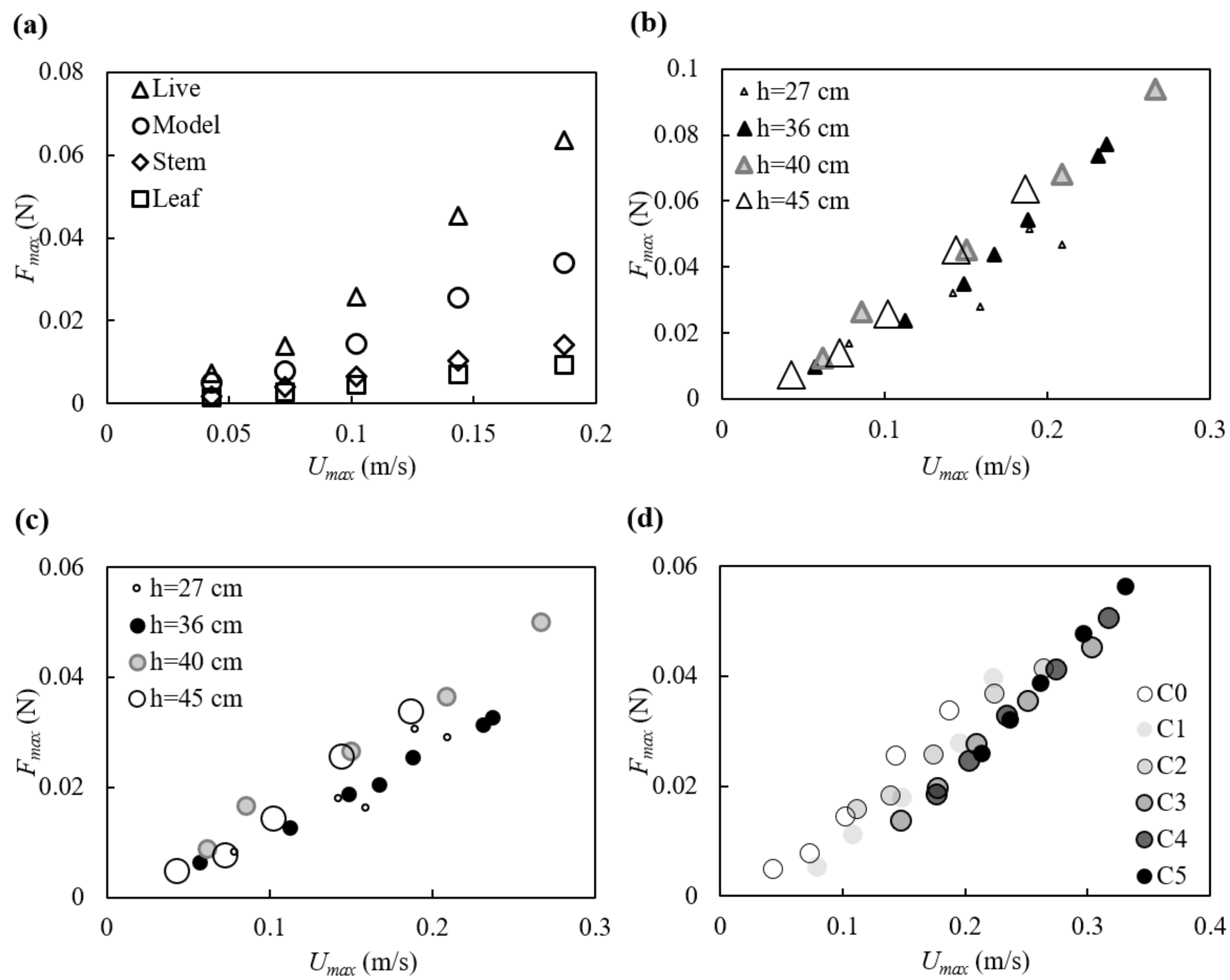

Fig. 6 maximum force on the plant plotted against the maximum horizontal velocity for (a) all plants at h = 45 cm, (b) the live plant and (c) the model plant under pure waves, (d) the model plant at h = 45 cm under combined current and waves with increasing current intensity labeled by C0 to C5. All the cases shown are associated with wave frequency f = 0.5 Hz. The uncertainty in the force measurements, not shown in the figures, ranged from 0.001 to 0.002 N based on the standard deviations of force in each wave phase.

3.2 Canopy velocity structure and turbulence

The canopy velocity structure and turbulence were altered by the plant drag, which in turn affected the dissipation of wave energy. Fig. 7 shows a few examples of the turbulence and velocity structure of the ME test. First, for pure current, the presence of the canopy significantly modified both the flow structure and turbulent intensity (Fig. 7a). The time-mean velocity u_m at P1 (2 m upstream of the meadow) exhibited a boundary-layer velocity profile (circles in Fig. 7a2), and the

TKE was essentially uniform, with a slight increase near the bed (circles in Fig. 7a1). The canopy resistance reduced u_m within the canopy height by a factor of 0.29 and redirected the time-mean flow above the canopy, forming a shear layer extending from the top of the stems toward the free surface (Fig. 7a2). Within the canopy, the magnitude of the horizontal velocity was negatively correlated with the distribution of plant frontal area (Nepf, 2012). Specifically, a greater time-mean velocity was observed near the bed (Fig. 7a2) where the plant frontal area was smaller (Fig. 2b). Considering that the velocity is zero at the bed, the velocity profile u_m exhibited an "S" shape at P2 (2.46 m inside the meadow). The time-mean velocity u_m at five lateral locations within the canopy (y1 to y5, red pluses in Fig. 3b) were the same within uncertainty, but the TKE was maximum directly upstream of a plant (P2_y1 and P2_y5) and minimum directly downstream of a plant (P2_y3). The maximum TKE was observed near the top of the canopy due to shear production associated with the strong vertical gradient in velocity (Fig. 7a2).

For pure waves, the turbulence intensity was maximum near the free surface and decreased with distance from the surface at P1 (circles in Fig. 7b1). Note that the time-mean velocity can be slightly negative in a closed flume, reflecting the return current that develops to balance the mass transport associated with the Stokes draft (Monismith, 2020), and its magnitude increases with distance from the bottom (Fig. 7b2). The presence of the canopy reduced the wave orbital velocity u_w slightly due to the wave energy dissipation by the plants (Fig. 7b3) and adjusted the time-mean velocity to a more uniform profile (Fig. 7b2). Compared to TKE measured at P1, the turbulent intensity at P2 was larger within the canopy, but similar near the top of the canopy (Fig. 7b1). Specifically, above the canopy height, TKE was primarily generated by the mean shear production, and the similar TKE at P1 and P2 can be explained by the comparable time-mean velocity profiles, i.e., comparable shear. Within the canopy, TKE was mainly generated by the plant form drag, such that TKE was obviously larger compared to P1.

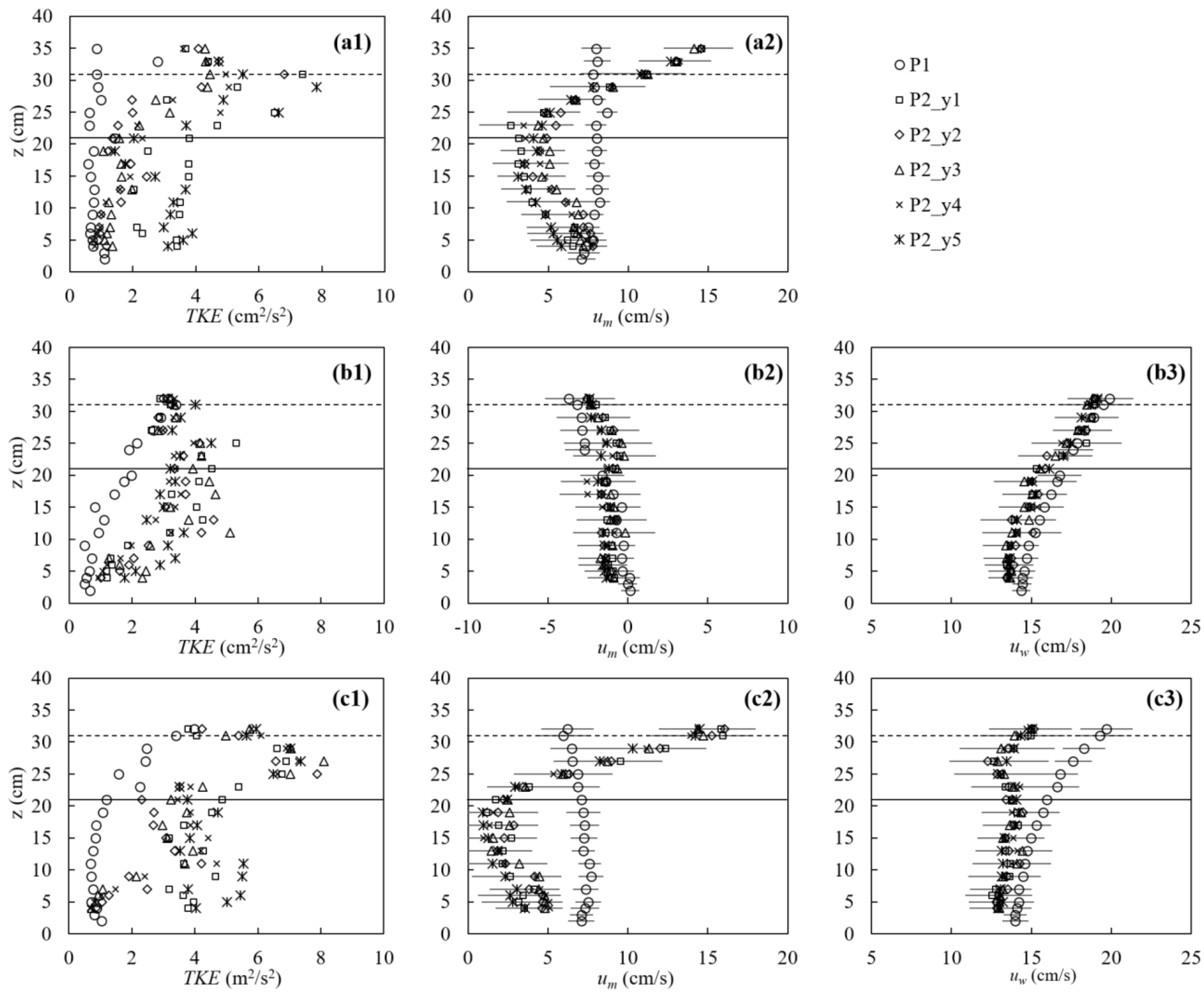

Fig. 7 The turbulent kinetic energy (left), horizontal time-mean velocity (middle), and wave orbital velocity (right column) for (a) pure current (h40_C2, U_m = 7.7 cm/s), (b) pure waves (h40_f07_W5, U_m = -1.8 cm/s, U_w = 16.7 cm/s), and (c) combined current and waves (h40_f07_C2W5, U_m = 7.0 cm/s, U_w = 15.6 cm/s). For the cases shown, water depth h = 40 cm. The measurements were made at P1 (2 m in front of the meadow at flume central) and P2 (2.46 m in the meadow) at five lateral positions y1 to y5 shown as red plus signs in Fig. 3b. The horizontal bars indicate the average standard deviation within each phase bins. The solid and dashed horizontal lines indicate the stem height and erect canopy height, respectively.

Finally, consider the conditions with combined current and waves (Fig. 7c). Upstream of the canopy (position P1, open circles in Fig. 7), the time-mean velocity u_m (Fig. 7c2) and wave velocity u_w (Fig. 7c3) exhibited the same vertical profile shape as that observed for the pure current (Fig. 7a2) and pure wave conditions (Fig. 7b3), respectively, and TKE (Fig. 7c1) was similar in magnitude to the pure wave condition (Fig. 7b1). This might be explained by time-mean velocity gradients (Fig. 7c2 and 7b2), which feed shear-production of turbulence and are similar in pure wave and combined wave-current conditions. Within the meadow (P2), adding current resulted in greater decrease in u_w and a more uniform profile (Fig. 7c3), compared to that under pure waves (Fig. 7b3). Smaller in-canopy wave orbital velocity was explained by greater plant drag (positively related to $u_m + u_w$ as in Fig. 6) and hence greater wave energy dissipation under combined conditions than the same pure wave (Zhang and Nepf, 2021a). Similarly, stronger plant resistance under combined current and waves resulted in a greater reduction in time-mean velocity within the canopy, relative to upstream, compared to pure current conditions (Fig. 7c2). Specifically, for the combined wave-current conditions, u_m within the canopy (roughly z <30 cm) at P2 was reduced by a factor of 0.42, compared to u_m at P1. Whereas for the pure current condition the reduction was only a factor of 0.29. Finally, in combined wave-current conditions, the TKE within the meadow (P2) was greater than TKE for either the pure current or pure wave conditions (comparing the left column in Fig. 7). This was consistent with the greater reduction in in-canopy current and greater dissipation of wave energy, because energy lost from time-mean and wave energy is converted into turbulent kinetic energy. In addition, in the combined wave-current conditions two regions of high TKE were observed, one near the top of the canopy, associated with shear-generated turbulence and consisted with the pure current condition, and a second within the lower canopy, associated with plant element-generated turbulence (Fig. 7c1).

In addition to the time-mean velocity, wave-orbital velocity, and turbulent kinetic energy, the time series for each velocity component (u, v, w) as both raw data and phase-averaged velocity for all ME are contained in the dataset. This dataset can be used to describe the physical mechanisms associated with current-wave-vegetation interaction.

3.3 Wave decay over salt marsh meadow

ME measured the free surface displacement at 2000 Hz, with a spatial interval of 10 or 15 cm along the meadow length. These data can be used to examine the wave amplitude dissipation (as in Zhang et al., 2021, 2022; Zhang and Nepf, 2021a) and wave shape transformation over a salt marsh meadow. The wave decay coefficient, K_D, increased with decreasing water depth and decreasing wave amplitude (Fig. 8). For a constant water depth (circles in Fig. 8), as wave period increased from T_w =1.12 s to 1.44, K_D increased, but then remained the same within uncertainty between T_w = 1.44 and 2.01 s. The dependence of K_D on water depth, wave amplitude, and wave period can be explained by how these parameters affect the fluid velocity and drag on the plant. First, for the same a_w and T_w, U_w increases with decreasing h, generating greater plant drag and thus greater wave energy dissipation as water depth decreases. Second, for a constant depth (h = 45 cm) and wave amplitude, an increase in wave period (here, T_w =1.11, 1.44, and 2.01 s) produces a decrease in dimensionless wave number kh = 1.55, 1.08, and 0.77, respectively. This decrease in kh is associated with wave velocity profile that is increasingly more uniform, producing larger depth-averaged velocity magnitude (see Figure B.1 in Zhang et al., 2022). Finally, with constant depth and wave period, an increase in wave amplitude results in greater plant motion within the wave cycle, which leads to a greater reduction in the plant drag (due to greater plant reconfiguration) and wave dissipation. Detailed mechanisms and scaling analysis was provided in Zhang et al. (2022).

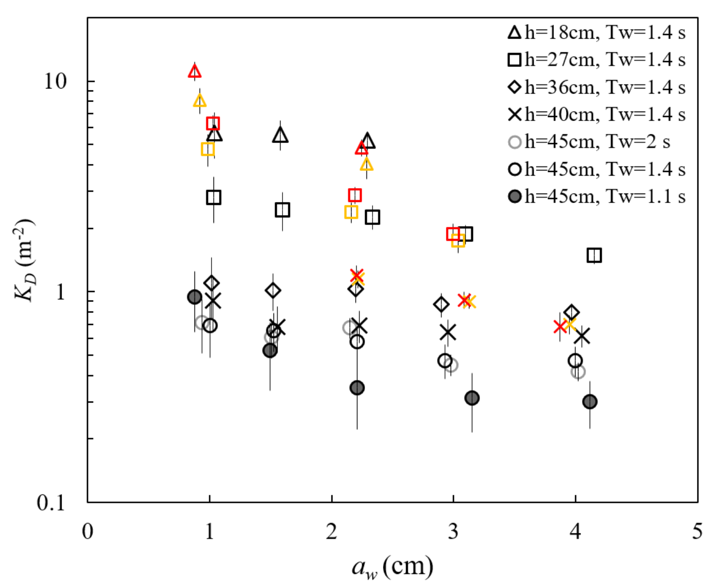

Fig. 8 Wave decay coefficients K_D for all cases reported in the (Zhang and Nepf, 2021a; Zhang et al., 2021, 2022). The yellow and red symbols indicated waves with small (U_c = 4.7 cm/s) and larger (U_c = 7.8 cm/s) following current, respectively. The vertical bars indicate uncertainty in K_D. (adopted from Figure 4a in Zhang et al., 2021)

Adding a following current tended to increase wave dissipation. For the same water depth and wave period, K_D increased with increasing current magnitude (red and yellow symbols in Fig. 8), compared to pure wave conditions (black symbols in Fig. 8) with similar wave amplitude. The effect of a following current increasing wave dissipation is shown more clearly in Fig. 9, which shows the ratio of wave decay coefficient in combined current and wave ($K_{D,cw}$) normalized by the value in pure waves ($K_{D,pw}$). Generally, as current increased, $K_{D,cw}/K_{D,pw}$ increased above 1. There were a few exceptions for U_c/U_w < 0.6, for which adding a weak current slightly reduced the wave decay coefficient, i.e., $K_{D,cw}/K_{D,pw}$ < 1. This opposite effect of current on wave decay has been reported in a few previous studies (Hu et al., 2014; Li and Yan, 2007; Yin et al., 2020; Paul et al., 2012; Losada et al., 2016; Zhao et al., 2020). Paul et al. (2012) attributed the reduction in wave dissipation with current mainly to an observed reduction in plant motion. However, for rigid canopies, following current was also observed to reduce wave dissipation when U_c/U_w was smaller than a transition value of 0.65 to 1.25 (Hu et al., 2014) and 0.37 to 1.54 (Yin et al., 2020), but larger currents increased wave dissipation above pure wave values ($K_{D,cw}/K_{D,pw} > 1$, Hu et al., 2014; Li and Yan, 2007; Yin et al., 2020). With an opposing current, wave dissipation was enhanced and to a higher degree compared to that of the following current of similar magnitude (Hu et al., 2021).

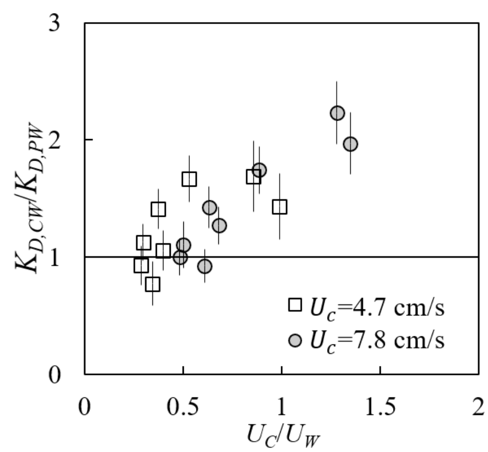

Fig. 9 Ratio of wave decay coefficients under combined condition to pure wave condition plotted against the ratio of current to wave velocity. (adopted from Figure 6a in Zhang and Nepf, 2021a)

Based on our laboratory measurements and theoretical analysis, we explained the different observed effects of current on wave dissipation as the result of the following competing mechanisms. First, consider that the wave energy was only dissipated by plants, the time rate of energy dissipation scales with plant drag and canopy total velocity $E_D \sim F_D U$. Adding current increases the total fluid velocity (Fig. 7) and thus the total plant force (Fig. 6), resulting in a greater wave energy dissipation, compared to the same pure wave. Second, the influence of current on wave dissipation is further modulated by the effect of plant resistance on the time-mean canopy flow structure (Fig. 7). In particular, the time-mean velocity within the canopy is significantly reduced compared to velocity upstream of the canopy at the same distance from the bed (P1 in Fig. 7). A reduction in time-mean velocity in the canopy, relative to the depth-averaged, time-mean velocity, decreases the impact of current on wave decay. Because the in-canopy current has a greater reduction for a denser canopy, the influence of current on wave decay is diminished for a denser canopy, relative to a sparser canopy. Third, current changes the speed of wave energy propagation, i.e., the wave group velocity $C_g = C_{g,pw} + U_c$, which connects the time-rate of wave energy dissipation to the spatial rate of wave energy dissipation (represented by K_D). For the same $|U_c|$ and plant drag (associated with the same E_D), an opposing (following) current decreases (increases) C_g and generates larger (smaller) K_D (spatial rate of amplitude decay).

For the experiments describe here, conducted in a finite length channel, the time-mean velocity was slightly negative for pure waves (Fig. 7b2), such that adding small following current could lead to a decrease in the magnitude of time-mean velocity. Further increase in the current magnitude would increase the magnitude of time-mean and total velocity, which is why the present and previous studies (Hu et al., 2014; Yin et al., 2020) observed a reduction in K_D only under small following current, with a larger following current increasing K_D, compared to the same pure wave. The greater increase in K_D under an opposing current than under a following current with the same magnitude, as observed in (Hu et al., 2014; Yin et al., 2020), can be explained by the effect of current direction on wave group velocity (the third mechanism above). The decrease in K_D observed in highly flexible seagrass mimics (Paul et al., 2012) under following current might be explained by the weaker increase in plant drag and canopy flow velocity (associated with limited increase in the time-rate energy dissipation), and the decrease in K_D due to an increase in wave group velocity C_g (the third mechanism above), compared to pure wave conditions. Specifically, increasing current led to a more pronated plant posture and decreased force on the flexible leaves, compared to a leaf under the same pure wave (see Figure 6 and table 1 in Lei and Nepf, 2019a). Further, the time-mean velocity within the canopy height was smaller under combined current and waves than for pure current of the same magnitude (see Fig. 7a2 and 7c2), and the canopy time-mean velocity was further reduced by the decrease in canopy height due to plant reconfiguration, both because the deflection increased the plant solid volume fraction within the canopy, and because in-canopy velocity decreases with increasing degree of canopy submergence (Chen et al., 2013).

4. Data availability

All instrument measured data presented in this paper are available from Figshare (https://doi.org/10.6084/m9.figshare.24117144; Zhang and Nepf, 2023a). The repository includes the raw time series, phase-averaged, and various statistical metrics (time-mean, maximum, minimum) of force, surface displacement, and velocity. A "readme.pdf" file included in the repository provides additional data instructions. To enhance the accessibility of the data, we prepared the data in two formats, i.e., the SMCW.mat file and the SMCW.nc file, both of which were included in the Figshare link. The SMCW.mat can be directly imported into MATLAB and Python. The SMCW.nc file is a NetCDF file with metadata that can be accessed by C, C++, Fortran, Python as well as Matlab. The plant motion recorded in the individual plant experiments can be found at: https://doi.org/10.6084/m9.figshare.24117324; Zhang and Nepf, 2023b. For each plant, a video with the same frame but including a ruler was included to give a scale of the plant motion.

5. Recommendations for data reuse

5.1 Plant dynamic model validation

The plant motion videos, phase-resolving plant drag, free surface displacement, and 3D velocity data can be used to validate phase-resolving plant dynamic models. The time-averaged force and velocity statistics can be used to validate phase-averaged plant drag models (as in Zhang and Nepf, 2021b, 2022). This dataset includes data not included in Zhang and Nepf (2021 and 2022) which is associated with strongly nonlinear waves, which reveal the nonlinear effects on plant motion and drag.

The measurements captured a phase lag between the plant force and wave motion (reflected by the free surface displacement). The presence of a following current tended to increase the magnitude of this phase lag (Fig. 5). The dataset in Hu et al. (2021) also contained time lags between the wave (velocity) and force data (Figure 5 in their paper). However, their wave and force data were not measured simultaneously, so the source of phase lag was unclear. Using a high-resolution synchronization method, Jacobsen et al. (2019) were able to capture the phase lag between the motion of a single flexible leaf and the fluid velocity, which informed an important knowledge gap in describing the physical cause of the observed phase lag. The present dataset can be used to deepen our understanding of the plant motion and force in response to waves with and without current in high temporal resolution.

5.2 Flow structure within salt marsh meadow

The drag associated with a canopy has long been known to modify the vertical structure of current and wave velocity (Chen et al., 2013; Lowe et al., 2005; Zeller et al., 2015; Lei and Nepf, 2021), but few data have been reported under combined current and waves. The present dataset directly compares the flow structure within a marsh canopy under pure current, pure wave, and their combination. Lowe et al. (2005) showed that a submerged canopy is more effective in reducing the time-mean velocity than the wave orbital velocity. They developed a 2-layer model to predict the canopy wave orbital velocity without considering the influence of current. Zeller et al. (2015) developed a prediction for the canopy total velocity under combined current and waves. However, their model was only validated using five flow conditions in a rigid canopy. Further, previous studies of canopy velocity structure seldom compare the reduction of time-mean and wave orbital velocity using laboratory data measured under current and waves acting alone and in combination. The present ME dataset provides high resolution velocity profiles upstream (single profile) and within (five lateral locations) a meadow under combined current and wave conditions (e.g., Fig. 7). The dataset covers water depth to plant height ratios from emergent to submerged and velocity ratios $U_c/U_w = 0.16$ to 4.7. Measurements were also made using the same current and wave acting alone. This dataset can be utilized to study the interaction between current and waves. In particular, the canopy time-mean velocity was reduced when waves were present (Fig. 7b2 and c2), suggesting that the waves enhanced the time-mean plant drag. The dataset can be used to validate theoretical and numerical models that predict canopy current and wave velocity.

5.3 Turbulent kinetic energy due to salt marsh

As shown in Fig.7 and described in section 3.2, the presence of marsh plants significantly enhanced turbulence intensity. For current over bare beds, turbulence is generated by spatial gradients in time-mean velocity (shear production), and the TKE is essentially uniform, except very close to the bed (circles in Fig. 7a1). However, when waves are presented, TKE was maximum near free surface and decreased away from the surface (circles in Fig. 7b1 and c1), possibly due to time-mean shear introduced by the return current associated with wave conditions (circles in Fig. 7b3 and c3). Within the meadow, the TKE varied with position relative to individual plants. TKE was largest under combined current and wave conditions (compare the left column in Fig. 7), with turbulence peaks observed near the top of the canopy, associated with shear-production by the time-mean current, and also within the canopy, associated with turbulence production in the wakes of individual plants (Fig. 7c1). This dataset can be used to develop and validate models to predict canopy turbulence (e.g., Xu and Nepf, 2020) and for use in numerical models (e.g., Tang and Lin, 2021).

5.4 Wave decay over salt marsh meadow

The meadow experiments (ME) measured the free surface displacement along the length of the meadow with a horizontal interval of 10 and 15 cm, which included 18 to 26 points within one wave length (see Figure C.1 in Zhang et al., 2022). The raw time-series data can be utilized to analyze the transformation of wave shape, including wave skewness and wave asymmetry, over salt marshes. The wave shape is a crucial parameter when describing wave-driven sediment motion and hence important for the study of coast stability within salt marsh regions.

The wave dissipation dataset presented here adds to the dataset reported in Hu et al. (2021), expanding the range of conditions. Specifically, Hu et al. (2021) reported wave decay data over rigid cylinders, while the present dataset provides wave decay over model plants with more realistic morphology and flexibility. The dataset can be applied to validate phase-averaged (e.g., Garzon et al., 2019a; Smith et al., 2016) and phase-resolving coastal models (e.g., Chen and Zou, 2019; Mattis et al., 2019) in predicting the wave energy reduction by salt marshes.

Author contributions. XXZ designed the experiments, conducted the experiments and collected the raw data. XXZ prepared the manuscript, HN reviewed and edited the manuscript.

Competing interests. The contact author has declared that neither they nor their coauthors have any competing interests.

Acknowledgments. We thank Dr. Jiarui Lei for his guidance with the experimental equipment.

Financial support. This study was supported by the National Key Research and Development Program of China (No. 2022YFE0136700). Xiaoxia Zhang was supported by the China Scholarship Council. The project also received support from the US National Science Foundation under EAR 1659923.

6. References

Barbier, E. B., Hacker, S. D., Kennedy, C., Koch, E. W., Stier, A. C., and Silliman, B. R.: The value of estuarine and coastal ecosystem services, Ecological Monographs, 81, 169–193, https://doi.org/10.1890/10-1510.1, 2011.

Boesch, D. F. and Turner, R. E.: Dependence of fishery species on salt marshes: The role of food and refuge, Estuaries, 7, 460–468, https://doi.org/10.2307/1351627, 1984.

Borges, F. O., Santos, C. P., Paula, J. R., Mateos-Naranjo, E., Redondo-Gomez, S., Adams, J. B., Caçador, I., Fonseca, V. F., Reis-Santos, P., Duarte, B., and Rosa, R.: Invasion and Extirpation Potential of Native and Invasive Spartina Species Under Climate Change, Front. Mar. Sci., 8, 696333, https://doi.org/10.3389/fmars.2021.696333, 2021.

Chen, H. and Zou, Q.: Eulerian–Lagrangian flow-vegetation interaction model using immersed boundary method and OpenFOAM, Advances in Water Resources, 126, 176–192, https://doi.org/10.1016/j.advwatres.2019.02.006, 2019.

Chen, Z., Jiang, C., and Nepf, H.: Flow adjustment at the leading edge of a submerged aquatic canopy, Water Resour. Res., 49, 5537–5551, https://doi.org/10.1002/wrcr.20403, 2013.

Elschot, K., Bouma, T. J., Temmerman, S., and Bakker, J. P.: Effects of long-term grazing on sediment deposition and salt-marsh accretion rates, Estuarine, Coastal and Shelf Science, 133, 109–115, https://doi.org/10.1016/j.ecss.2013.08.021, 2013.

Garzon, J. L., Miesse, T., and Ferreira, C. M.: Field-based numerical model investigation of wave propagation across marshes in the Chesapeake Bay under storm conditions, Coastal Engineering, 146, 32–46, https://doi.org/10.1016/j.coastaleng.2018.11.001, 2019a.

Garzon, J. L., Maza, M., Ferreira, C. M., Lara, J. L., and Losada, I. J.: Wave attenuation by Spartina saltmarshes in the Chesapeake Bay under storm surge conditions, J. Geophys. Res. Oceans, 124, 5220–5243, https://doi.org/10.1029/2018JC014865, 2019b.

Gosselin, F., De Langre, E., and Machado-Almeida, B. A.: Drag reduction of flexible plates by reconfiguration, J. Fluid Mech., 650, 319–341, https://doi.org/10.1017/S0022112009993673, 2010.

Harder, D. L., Speck, O., Hurd, C. L., and Speck, T.: Reconfiguration as a prerequisite for survival in highly unstable flow-dominated habitats, J Plant Growth Regul, 23, 98–107, https://doi.org/10.1007/s00344-004-0043-1, 2004.

Hu, Z., Suzuki, T., Zitman, T., Uittewaal, W., and Stive, M.: Laboratory study on wave dissipation by vegetation in combined current–wave flow, Coastal Engineering, 88, 131–142, https://doi.org/10.1016/j.coastaleng.2014.02.009, 2014.

Hu, Z., Lian, S., Wei, H., Li, Y., Stive, M., and Suzuki, T.: Laboratory data on wave propagation through vegetation with following and opposing currents, Earth Syst. Sci. Data, 13, 4987–4999, https://doi.org/10.5194/essd-13-4987-2021, 2021.

Huai, W., Li, S., Katul, G. G., Liu, M., and Yang, Z.: Flow dynamics and sediment transport in vegetated rivers: A review, J Hydrodyn, 33, 400–420, https://doi.org/10.1007/s42241-021-0043-7, 2021.

Jacobsen, N. G., Bakker, W., Uijttewaal, W. S. J., and Uittenbogaard, R.: Experimental investigation of the wave-induced motion of and force distribution along a flexible stem, J. Fluid Mech., 880, 1036–1069, https://doi.org/10.1017/jfm.2019.739, 2019.

Jalonen, J. and Järvelä, J.: Impact of tree scale on drag: Experiments in a towing tank, in: Proceedings of 2013 IAHE world Congress, 2013.

Keulegan, G. H. and Carpenter, L. H.: Forces on cylinders and plates in an oscillating fluid, J. RES. NATL. BUR. STAN., 60, 423, https://doi.org/10.6028/jres.060.043, 1958.

Knutson, P. L., Brochu, R. A., Seeling, W. N., and Margaret, I.: Wave damping in Spartina alterniflora marsh, Wetlands, 2, 87–104, 1982.

Lei, J. and Nepf, H.: Blade dynamics in combined waves and current, Journal of Fluids and Structures, 87, 137–149, https://doi.org/doi:10.1016/j.jfluidstructs.2019.03.020, 2019a.

Lei, J. and Nepf, H.: Wave damping by flexible vegetation: Connecting individual blade dynamics to the meadow scale, Coastal Engineering, 147, 138–148, https://doi.org/10.1016/j.coastaleng.2019.01.008, 2019b.
Lei, J. and Nepf, H.: Evolution of flow velocity from the leading edge of 2-D and 3-D submerged canopies, J. Fluid Mech., 916, A36, https://doi.org/10.1017/jfm.2021.197, 2021.
Li, C. W. and Yan, K.: Numerical investigation of wave–current–vegetation interaction, Journal of Hydraulic Engineering, 133, 794–803, https://doi.org/10.1061/(ASCE)0733-9429(2007)133:7(794), 2007.
Losada, I. J., Maza, M., and Lara, J. L.: A new formulation for vegetation-induced damping under combined waves and currents, Coastal Engineering, 107, 1–13, https://doi.org/10.1016/j.coastaleng.2015.09.011, 2016.
Lowe, R. J., Koseff, J. R., and Monismith, S. G.: Oscillatory flow through submerged canopies: 1. Velocity structure, Journal of Geophysical Research: Oceans, 110, https://doi.org/10.1029/2004JC002788, 2005.
Luhar, M. and Nepf, H. M.: Flow-induced reconfiguration of buoyant and flexible aquatic vegetation, Limnol. Oceanogr., 56, 2003–2017, https://doi.org/10.4319/lo.2011.56.6.2003, 2011.
Luhar, M. and Nepf, H. M.: Wave induced dynamics of flexible blades, Journal of Fluids and Structures, 61, 20–41, https://doi.org/10.1016/j.jfluidstructs.2015.11.007, 2016.
Mattis, S. A., Kees, C. E., Wei, M. V., Dimakopoulos, A., and Dawson, C. N.: Computational model for wave attenuation by flexible vegetation, J. Waterway, Port, Coastal, Ocean Eng., 145, 04018033, https://doi.org/10.1061/(ASCE)WW.1943-5460.0000487, 2019.
Maza, M., Lara, J. L., Losada, I. J., Ondiviela, B., Trinogga, J., and Bouma, T. J.: Large-scale 3-D experiments of wave and current interaction with real vegetation. Part 2: Experimental analysis, Coastal Engineering, 106, 73–86, https://doi.org/10.1016/j.coastaleng.2015.09.010, 2015.
Monismith, S. G.: Stokes drift: theory and experiments, J. Fluid Mech., 884, F1, https://doi.org/10.1017/jfm.2019.891, 2020.
Morison, J. R., Johnson, J. W., and Schaaf, S. A.: The force exerted by surface waves on piles, Journal of Petroleum Technology, 2, 149–154, https://doi.org/10.2118/950149-G, 1950.
Mullarney, J. C. and Henderson, S. M.: Wave-forced motion of submerged single-stem vegetation, J. Geophys. Res., 115, C12061, https://doi.org/10.1029/2010JC006448, 2010.
Nepf, H. M.: Flow and transport in regions with aquatic vegetation, Annu. Rev. Fluid Mech., 44, 123–142, https://doi.org/10.1146/annurev-fluid-120710-101048, 2012.
Paul, M., Bouma, T., and Amos, C.: Wave attenuation by submerged vegetation: combining the effect of organism traits and tidal current, Mar. Ecol. Prog. Ser., 444, 31–41, https://doi.org/10.3354/meps09489, 2012.
Pidgeon, E.: Carbon sequestration by coastal marine habitats: Important missing sinks, in: The Management of Natural Coastal Carbon Sinks, 2009.
Schoutens, K., Heuner, M., Minden, V., Schulte Ostermann, T., Silinski, A., Belliard, J.-P., and Temmerman, S.: How effective are tidal marshes as nature-based shoreline protection throughout seasons, Limnol. Oceanogr., 64, 1750–1762, https://doi.org/10.1002/lno.11149, 2019.
Schoutens, K., Heuner, M., Fuchs, E., Minden, V., Schulte-Ostermann, T., Belliard, J.-P., Bouma, T. J., and Temmerman, S.: Nature-based shoreline protection by tidal marsh plants depends on trade-offs between avoidance and attenuation of hydrodynamic forces, Estuarine, Coastal and Shelf Science, 236, 106645, https://doi.org/10.1016/j.ecss.2020.106645, 2020.
Schoutens, K., Luys, P., Heuner, M., Fuchs, E., Minden, V., Schulte Ostermann, T., Bouma, T., Van Belzen, J., and Temmerman, S.: Traits of tidal marsh plants determine survival and growth response to hydrodynamic forcing: implications for nature-based shoreline protection, Mar. Ecol. Prog. Ser., 693, 107–124, https://doi.org/10.3354/meps14091, 2022.
Schutten, J. and Davy, A. J.: Predicting the hydraulic forces on submerged macrophytes from current velocity, biomass and morphology, Oecologia, 123, 445–452, https://doi.org/10.1007/s004420000348, 2000.

Smith, J. M., Bryant, M. A., and Wamsley, T. V.: Wetland buffers: numerical modeling of wave dissipation by vegetation, Earth Surf. Process. Landforms, 41, 847–854, https://doi.org/10.1002/esp.3904, 2016.

Tang, X., Lin, P., Liu, P. L. -F., and Liu, X.: Numerical and experimental studies of turbulence in vegetated open-channel flows, Environmental Fluid Mechanics, 2021.

van Veelen, T. J., Fairchild, T. P., Reeve, D. E., and Karunarathna, H.: Experimental study on vegetation flexibility as control parameter for wave damping and velocity structure, Coastal Engineering, 157, 103648, https://doi.org/10.1016/j.coastaleng.2020.103648, 2020.

Vuik, V., Jonkman, S. N., Borsje, B. W., and Suzuki, T.: Nature-based flood protection: The efficiency of vegetated foreshores for reducing wave loads on coastal dikes, Coastal Engineering, 116, 42–56, https://doi.org/10.1016/j.coastaleng.2016.06.001, 2016.

Whittaker, P., Wilson, C., Aberle, J., Rauch, H. P., and Xavier, P.: A drag force model to incorporate the reconfiguration of full-scale riparian trees under hydrodynamic loading, Journal of Hydraulic Research, 51, 569–580, https://doi.org/10.1080/00221686.2013.822936, 2013.

Xu, Y. and Nepf, H.: Measured and predicted turbulent kinetic energy in flow through emergent vegetation with real plant morphology, Water Resour. Res., 56, https://doi.org/10.1029/2020WR027892, 2020.

Yin, Z., Wang, Y., Liu, Y., and Zou, W.: Wave attenuation by rigid emergent vegetation under combined wave and current flows, Ocean Engineering, 213, 107632, https://doi.org/10.1016/j.oceaneng.2020.107632, 2020.

Ysebaert, T., Yang, S., Zhang, L., He, Q., Bouma, T. J., and Herman, P. M. J.: Wave attenuation by two contrasting ecosystem engineering salt marsh macrophytes in the intertidal pioneer zone, Wetlands, 31, 1043–1054, https://doi.org/10.1007/s13157-011-0240-1, 2011.

Zeller, R. B., Zarama, F. J., Weitzman, J. S., and Koseff, J. R.: A simple and practical model for combined wave-current canopy flows, J. Fluid Mech., 767, 842–880, https://doi.org/10.1017/jfm.2015.59, 2015.

Zhang, X. and Nepf, H.: Flow-induced reconfiguration of aquatic plants, including the impact of leaf sheltering, Limnology and Oceanography, 65, 2697–2712, https://doi.org/org/10.1002/lno.11542, 2020.

Zhang, X. and Nepf, H.: Wave damping by flexible marsh plants influenced by current, Phys. Rev. Fluids, 6, 100502, https://doi.org/10.1103/PhysRevFluids.6.100502, 2021a.

Zhang, X. and Nepf, H.: Wave-induced reconfiguration of and drag on marsh plants, Journal of Fluids and Structures, 100, 103192, https://doi.org/10.1016/j.jfluidstructs.2020.103192, 2021b.

Zhang, X. and Nepf, H.: Reconfiguration of and drag on marsh plants in combined waves and current, Journal of Fluids and Structures, 110, 103539, https://doi.org/10.1016/j.jfluidstructs.2022.103539, 2022.

Zhang, X., Lin, P., Gong, Z., Li, B., and Chen, X.: Wave attenuation by Spartina alterniflora under macro-tidal and storm surge conditions, Wetlands, 40, 2151–2162, https://doi.org/10.1007/s13157-020-01346-w, 2020.

Zhang, X., Lin, P., and Nepf, H.: A simple wave damping model for flexible marsh plants, Limnology and Oceanography, 66, 4182–4196, https://doi.org/doi: 10.1002/lno.11952, 2021.

Zhang, X., Lin, P., and Nepf, H.: A wave damping model for flexible marsh plants with leaves considering linear to weakly nonlinear wave conditions, Coastal Engineering, 175, 104124, https://doi.org/10.1016/j.coastaleng.2022.104124, 2022.

Zhao, C., Tang, J., and Shen, Y.: Experimental study on solitary wave attenuation by emerged vegetation in currents, Ocean Engineering, 220, 108414, https://doi.org/10.1016/j.oceaneng.2020.108414, 2020.

Zhu, L., Zou, Q., Huguenard, K., and Fredriksson, D. W.: Mechanisms for the asymmetric motion of submerged aquatic vegetation in waves: A consistent-mass cable model, J. Geophys. Res. Oceans, 125, e2019JC015517, https://doi.org/10.1029/2019JC015517, 2020.

Zhu, L., Chen, Q., Ding, Y., Jafari, N., Wang, H., and Johnson, B. D.: Towards a unified drag coefficient formula for quantifying wave energy reduction by salt marshes, Coastal Engineering, 180, 104256, https://doi.org/10.1016/j.coastaleng.2022.104256, 2023.